

Hydrodynamic effects on the liquid-hexatic transition of active colloids

G. Negro¹, C. B. Caporusso¹, P. Digregorio², G. Gonnella¹, A. Lamura³, A. Suma¹

¹ Dipartimento di Fisica, Università degli Studi di Bari and INFN, Sezione di Bari, via Amendola 173, Bari, I-70126, Italy

² Centre Européen de Calcul Atomique et Moléculaire (CECAM), Ecole Polytechnique Fédérale de Lausanne (EPFL), Batochimie, Avenue Forel 2, 1015 Lausanne, Switzerland

³ Istituto Applicazioni Calcolo, CNR, Via Amendola 122/D, I-70126 Bari, Italy

Received: date / Accepted: date

Abstract We study numerically the role of hydrodynamics in the liquid-hexatic transition of active colloids at intermediate activity, where motility induced phase separation (MIPS) does not occur. We show that in the case of active Brownian particles (ABP), the critical density of the transition decreases upon increasing the particle's mass, enhancing ordering, while self-propulsion has the opposite effect in the activity regime considered. Active hydrodynamic particles (AHP), instead, undergo the liquid-hexatic transition at higher values of packing fraction ϕ than the corresponding ABP, suggesting that hydrodynamics have the net effect of disordering the system. At increasing densities, close to the hexatic-liquid transition, we found in the case of AHP the appearance of self-sustained organized motion with clusters of particles moving coherently.

1 Introduction

Self-propelled particles (SPP) are the fundamental units of a broad class of theoretical models for active matter. In the context of SPP models, injected energy from the environment fuels a persistent motion of the single constituents, driving the system out of thermal equilibrium. Simplified models of SPP [1, 2, 3, 4] are of crucial importance, because they offer a minimal setup to explore some of the large variety of collective behaviours observed in nature for systems of motile living bodies at different length scales, from flocking of birds and fish [5], to swarming in bacterial colonies [6] and dynamics in cells' cytoskeleton [7].

Active Brownian Particles (ABP) models are very popular among SPP models [8, 9, 1]. Active colloids are usually spherical particles undergoing directed motion due to an active force, while both translational and rotational degrees of freedom are in contact with a stochastic thermal bath. Although the model is very simple, ABP show paradigmatic collective phenomena like motility-induced phase separation (MIPS) [10, 11, 12, 13] and are therefore very interesting in order to characterize the fundamental principles governing active matter systems. Moreover, ABP are of primary use for comparisons with experimental systems of synthetic micro-swimmers [13, 14], opening the perspectives for a systematic control of active systems and collective motion, with the purpose to exploit some of their unique features for tech-

nological uses, for instance in robotics [15, 16, 17], realisation of biological machines [18], or understanding of flocking intelligence [19, 20].

Of particular interest is the characterization of ABP in the dense regime, see e.g. spontaneous flow [21] or glassy behaviour [22, 23] in biological tissues, biofilms, cell monolayers [24, 25], and can be considered a target for the development of new materials [26]. In two dimensions (2D), ABP present ordering phase transitions when the density of the system is increased [27, 8, 9, 28], which are connected to those encountered for passive hard colloids [29, 30, 31]. At intermediate values of the self-propelling force, a liquid-hexatic critical transition is followed by a hexatic-solid transition, where the solid phase has quasi-long-range (QLR) positional and long-range (LR) orientational order, the hexatic phase has short-range (SR) positional and QLR orientational order, while the liquid phase is homogeneous and has SR positional and orientational order. This scenario is very similar to the theoretical Kosterlitz, Thouless, Halperin, Nelson, and Young (KTHNY) two-step scenario [32, 33, 34]. If activity is high enough, instead, MIPS takes place, as a phase separation between a dense phase and a gaseous one [8].

The aforementioned features of the ABP phase diagram have been well established in the context of over-damped motion and without an explicit underlying thermo-hydrodynamic bath. At the same time, there are other interesting questions that remain to be considered. The first question concerns

the role of particles mass, and in particular the interplay between inertial and active diffusion timescales, which can be varied independently [35, 36]. It has been pointed out in [37] that in three-dimensional active systems, inertia should attenuate the destabilizing effect of activity on the ordered phase. The presence of large inertia has also been shown to strongly affect the kinetic energy of the particles into the highly dense phase of MIPS [38], and to highly inhibit phase segregation [39]. However, the role of inertia in the context of dense ABP, and in particular how the particle's mass affects the hexatic phase, has not yet been characterized. The second question concerns the role of hydrodynamic interactions in the dense phase. Regarding the influence of hydrodynamics in MIPS, it is found that in 2D MIPS is suppressed [40, 41, 42], as hydrodynamics favour reorientation of particles' self propulsion direction, while in quasi-2D systems MIPS has been observed for low-density fluids [43] and not when the fluid was made incompressible [44, 42]. For elongated colloids, steric alignment and hydrodynamics show highly non-trivial interplay, such that MIPS is enhanced for pullers and suppressed for pushers [40].

As a first step in the direction of answering these two questions, we characterize how the critical density for the liquid-hexatic transition of active particles is modified, in an intermediate activity regime where MIPS does not occur for ABP, by i) the inertial effects due to mass changes, and ii) the presence of non-isotropic interactions between colloids introduced by hydrodynamics. Hydrodynamics has been implemented by using the multi-particle collision method [45, 46], which seamlessly integrate with the dynamics of active Brownian particles [47]. In particular, we implement thermal slip boundary conditions, decoupling colloids rotational diffusion from the solvent and test the consistency of this implementation with known benchmark tests. We focus here only on 2D systems where the rotational diffusion follows the same equations as for ABP. This allows us to have an active hydrodynamic particle (AHP) model with the same friction, temperature and rotational diffusion as the ABP model, providing a way to quantitatively compare them.

We find that changing the colloids mass and introducing hydrodynamic interactions affect the critical density at which the liquid-hexatic transition occurs. In particular, mass changes lower this density with respect to over-damped ABP, while hydrodynamics increases the critical density. We also find that the system with hydrodynamics undergoes a transition from a disorganized to a self-sustained flow regime upon increasing the density, with particles moving on the same direction at high densities.

The work is organized in the following way. In Sec. II we discuss the numerical methods and parameter choice for the ABP model and for the AHP model, with Sec. II C providing several tests for implementation of the latter model. In Sec. III A we discuss how the liquid-hexatic scenario changes by

varying the active colloids mass, while in Sec. III B we discuss the effects due to hydrodynamics interactions. Finally we draw some conclusions discussing the main findings.

2 Numerical methods

In this Section we describe the numerical models. We will start with the ABP model, which follows a Langevin equation and does not include hydrodynamic interactions. We will then describe the AHP model, where hydrodynamic is accounted explicitly, and provide some numerical tests of the implementation.

2.1 Active Brownian particles (ABP)

We consider a two-dimensional system with N_c disks of mass m_c and diameter σ_c in a square box size of side L . Each disk i has also an associated axis $\mathbf{n}_i = (\cos \theta_i(t), \sin \theta_i(t))$, where θ_i is the angle between the axis and the x-axis and which evolves over time. \mathbf{n}_i represents the direction in which the self-propulsion occurs.

The particles interact with each other via a short-ranged repulsive potential:

$$U(r) = 4\epsilon \left[\left(\frac{\sigma}{r} \right)^{64} - \left(\frac{\sigma}{r} \right)^{32} + \frac{1}{4} \right] \Theta(\sigma_c - r) \quad (1)$$

where r is the inter-particle distance between the center of masses of each colloid, $\Theta(r)$ is the Heaviside function ($\Theta(r) = 0$ for $r < 0$ and $\Theta(r) = 1$ for $r \geq 0$), and $\sigma = 2^{-1/32} \sigma_c$.

The evolution of the centre of mass of disks is described by a Langevin equation, with activity modelled as a force F_{act} of constant magnitude acting along the particle axis \mathbf{n}_i , while the propulsion axis changes its direction in time through a diffusion equation:

$$m_c \ddot{\mathbf{r}}_i = -\gamma \dot{\mathbf{r}}_i + F_{\text{act}} \mathbf{n}_i - \nabla_i \sum_{j \neq i} U(r_{ij}) + \xi_i, \quad (2)$$

$$\dot{\theta}_i = \eta_i, \quad (3)$$

where $i = 1, \dots, N_c$, $r_{ij} = |\mathbf{r}_i - \mathbf{r}_j|$ and γ is the damping coefficient. The terms ξ_i and η_i are Gaussian white noises that mimic the interaction with a thermal bath, with average zero and variance fixed by the fluctuation-dissipation theorem:

$$\langle \xi_{i\alpha}(t) \rangle = 0, \quad \langle \eta_i(t) \rangle = 0, \quad (4)$$

$$\langle \xi_{i\alpha}(t_1) \xi_{j\beta}(t_2) \rangle = 2k_B T \gamma \delta_{ij} \delta_{\alpha\beta} \delta(t_1 - t_2), \quad (5)$$

$$\langle \eta_i(t_1) \eta_j(t_2) \rangle = 2D_\theta \delta_{ij} \delta(t_1 - t_2), \quad (6)$$

where $\alpha, \beta = 1, 2$ are the indices of the spatial coordinates, T the temperature of the system, k_B the Boltzmann constant and D_θ the rotational diffusion coefficient. We express all the quantities in units of mass, length and energy (\bar{m} , $\bar{\sigma}$ and $\bar{\epsilon}$, respectively), with the time unit expressed as $\tau =$

$(\tilde{m}\tilde{\sigma}^2/\varepsilon)^{1/2}$. Note that we fix $\sigma_c = 1\tilde{\sigma}$, while m_c is varied with respect to the mass unit \tilde{m} . From now on we will drop the units for simplicity.

The density of the system is expressed in terms of the packing fraction $\phi = \pi\sigma_c^2 N_c/(4L^2)$, ratio between the surface occupied by the colloids and the total system surface L^2 . An important adimensional number, which measures the ratio between the active work required to move a particle by σ_c and the typical thermal energy $k_B T$, is the Péclet number $Pe = F_{act}\sigma_c/(k_B T)$. Another useful adimensional number is the active Reynolds number, which measures the ratio between inertial and viscous forces acting on the colloids, $Re_{act} = \frac{m_c F_a}{\sigma_c \gamma^2}$ [48].

The typical time scales for a single ABP are the inertial time $t_I = m_c/\gamma$ and the persistence time $t_p = 1/D_\theta$, with the latter signaling the crossover to the final diffusive regime and that depends only on the rate of rotational diffusion and not on the activity parameter. We can define a useful adimensional number as the ratio between t_I and t_p , to which we refer to hereafter as the persistence number $pn = t_I/t_p$.

We fix in our numerical simulations $\gamma = 10$, as previously done for ABP [8] where the choice $m_c = 1$ was adopted, which corresponds to limit inertial effects at small times $t_I = 0.1$. In the following we keep fixed γ and vary the disk mass m_c to consider different inertial contributions, $k_B T = 0.05$ and $D_\theta = 3k_B T/(\sigma_c^2 \gamma) = 0.015$. We fix $N_c = 16384$ and vary L in order to obtain the correct packing fraction ϕ . We use LAMMPS[49] to integrate numerically the equations of motion, using a timestep $\Delta t_c = 0.001$ and periodic boundary conditions. We fix the Péclet number to $Pe = 5, 10$ and 20 , and vary the packing fraction ϕ between 0.60 and 0.88 . Within the range of chosen parameters, Re_{act} is always smaller than one. For each set of parameters a single realization was considered which was run between 10^4 and 10^5 simulation time units after steady state was reached. In this time frame averaged quantities were computed.

2.2 Active hydrodynamics particles (AHP)

The ABP model described beforehand does not account explicitly for the solvent. In order to add this effect, we choose as model a mesoscopic method known as multi-particle collision (MPC) dynamics, first introduced in [45]. After briefly describing the MPC model, we will introduce two possible ways to couple solvent and disks, their dynamics and the specific parameters used for simulations. Tests of this implementation are presented in section 2.3.

2.2.1 Solvent dynamics

The solvent consists of N_s identical point-like particles of mass m_s embedded in a two-dimensional square box of size

L . Each particle i is characterized by a position \mathbf{r}_i and velocity \mathbf{v}_i , both of which are continuous variables. In this algorithm, the time is discretized in units Δt_s , and the evolution of the system is composed by two steps, propagation and collision, which are applied consecutively for each Δt_s .

In the propagation step, particles are freely streamed according to their velocities as

$$\mathbf{r}_i(t + \Delta t_s) = \mathbf{r}_i(t) + \mathbf{v}_i(t)\Delta t_s. \quad (7)$$

In order to perform the collision step, the system is partitioned into cells of a square lattice with mesh size σ_s . Each cell is the scattering area where a MPC occurs, which updates particles velocities according to the rule [45,50]

$$\mathbf{v}_i(t + \Delta t_s) = \mathbf{u}(t) + \Omega[\mathbf{v}_i(t) - \mathbf{u}(t)], \quad (8)$$

where $\mathbf{u} = (\sum_{i=1}^m \mathbf{v}_i)/m$ is the mean velocity of the m colliding particles in the cell, also assumed to be the macroscopic velocity of the fluid. Ω is a rotation matrix with angle $\pm\alpha$ ($0 < \alpha < \pi$). The angle α is fixed at the beginning of the simulation while its sign is assigned with equal probability to every cell at each time step. In each cell all the m relative velocities are rotated with the same angle. Linear momentum and kinetic energy are conserved under this dynamics.

The transport coefficients of this model can be analytically derived. In particular, for our purposes the kinematic viscosity ν_s and the self-diffusion coefficient D_s will be useful. In 2D the viscosity is equal to [51,52]:

$$\nu_s = \frac{\sigma_s^2}{2\Delta t_s} \left[\left(\frac{\lambda}{\sigma_s} \right)^2 \left(\frac{n_s}{(n_s - 1 + \exp(-n_s)) \sin^2(\alpha)} - 1 \right) + \frac{(n_s - 1 + \exp(-n_s))(1 - \cos(\alpha))}{6n_s} \right], \quad (9)$$

while the coefficient D_s is [53]:

$$D_s = \frac{\lambda^2}{2\Delta t_s} \left(\frac{2n_s}{(n_s - 1 + \exp(-n_s))(1 - \cos(\alpha))} \right), \quad (10)$$

where $n_s = N_s \sigma_s^2 / L^2$ is the average number of particles per cell and $\lambda = \Delta t_s \sqrt{k_B T / m_s}$ is the mean-free path.

2.2.2 Solvent-colloids coupling

The next step would be to integrate the solvent particles with the colloids, which means that we need to decide how to couple colloids and solvent dynamics. Different strategies are possible and a review for MPC with passive colloids can be found in [46]; here we adopted the one implemented in the LAMMPS software[47].

In this implementation colloids are evolved for n time-steps Δt_c , following the equation of motion (2) without the force terms ξ_i and $\gamma \mathbf{r}_i$, which accounted implicitly for the

thermal bath in the ABP model, and are substituted here by the MPC bath. Afterwards solvent particles are propagated for a timestep equal to $\Delta t_s = n\Delta t_c$. Note that both Δt_c and Δt_s are expressed in the same time unit as in the ABP model. Before computing the collision (8), the algorithm checks if solvent particles are overlapping with disks having diameter σ_c and mass m_c , that is if the position of point-like solvent particles is inside the disks area. In this case, an exchange of momentum occurs, followed by a change in the position of solvent particles to place them out of the colloids, and, finally, the collision step for solvent particles is applied.

The exchange of momentum is decided by the proper colloid–solvent boundary condition (BC) adopted, which can be either no-slip or slip. No-slip BC means that both linear and angular momentum are exchanged between colloid and solvent particles[54], while for slip BC only linear momentum is transferred as in the case with radial interactions [50]. Several implementations of the BC are available, such as the so called thermal BC [55] and the bounce-back collision rule[56]. The latter, used in the case of no-slip BC, requires the use of phantom particles inside the colloid while the former does not. Here we choose the thermal BC method, described below for the slip and no-slip cases, as it is in general useful under forced flow conditions, like the case of active particles, and is particularly suited when the solvent mean free path is much smaller than the disk radius [57,58].

In the no-slip thermal BC, when a solvent particle of velocity \mathbf{v} overlaps with a disk, it is moved back to the disk surface along the shortest vector \mathbf{r}_d and then streamed for a distance $\mathbf{v}'\Delta t_s\epsilon$, where \mathbf{v}' is the updated velocity and ϵ is a uniformly distributed random number in the interval $[0, 1]$ [59]. The new velocity \mathbf{v}' is divided in the normal v_N and tangential v_T velocity components with respect to the particle–colloid distance, and chosen according to the stochastic distributions

$$p_N(v_N) = (m_s v_N / k_B T) \exp(-m_s v_N^2 / 2k_B T), v_N > 0 \quad (11)$$

$$p_T(v_T) = \sqrt{m_s / 2\pi k_B T} \exp(-m_s v_T^2 / 2k_B T), \quad (12)$$

centred around the local velocity \mathbf{v}_d of the colloid surface, where $\mathbf{v}_d = \mathbf{V} + \boldsymbol{\omega} \times (\mathbf{r}_d - \mathbf{R})$, with \mathbf{R} being the position of the colloid centre, \mathbf{V} and $\boldsymbol{\omega}$ the linear and angular velocities of the colloid. Regarding the change in momentum for the colloid after the collision, all the linear and angular momenta variations of the overlapping solvent particles are summed up as $\Delta \mathbf{P} = \sum_s m_s (\mathbf{v} - \mathbf{v}')$ and $\Delta \mathbf{L} = \sum_s m_s (\mathbf{r}_d - \mathbf{R}) \times (\mathbf{v} - \mathbf{v}')$, and the linear and angular velocities of the colloid are updated as: $\mathbf{V}' = \mathbf{V} + \Delta \mathbf{P} / m_c$ and $\boldsymbol{\omega}' = \boldsymbol{\omega} + \Delta \mathbf{L} / I$ where $I = m_c \sigma_c^2 / 8$ is the moment of inertia of a disk. In case of high packing fraction of colloids, it may happen that a single solvent particle can scatter with several disks in the same timestep Δt_s . Ignoring such multiple collisions would cause an attractive depletion-like force between disks [59]. This effect can be kept under control allowing a maximum

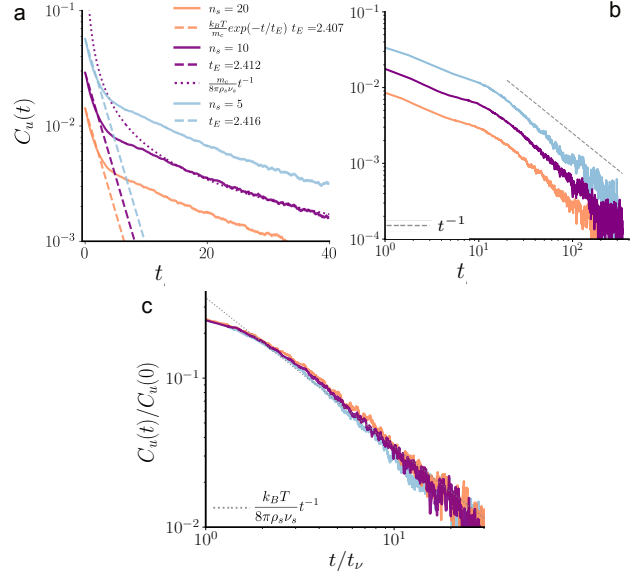


Fig. 1 VACF for different values of the number of solvent particles per cell n_s . Panels (a-c) show the VACF for three different values of n_s , namely $n_s = 20$ (blue curves) $n_s = 10$ (purple curves), and $n_s = 5$ (orange curves). For short times (a), the autocorrelation function shows a clear exponential decay, which overlaps well with the theoretical predictions of the the Enskog time, t_E , shown as a dashed line for each case. At late times (b) simulations show a long time tail t^{-1} (grey dashed lines in panels (b) and (c), and dotted purple line in panel (a)). All the data collapse to the same curve if time is rescaled by t_v (c).

number N_M of multiple collisions. It was found empirically that $N_M \simeq 10$ is the best choice to optimize computational speed and accuracy.

In the case of slip thermal BC, the tangential component of the fluid particle velocity is preserved during the scattering with disks; thus no torque is imparted to colloids. The normal component v_N of the solvent particle new velocity \mathbf{v}' is sampled from a Gaussian distribution according to the distribution of Eq. (11) which is centered around the disk velocity \mathbf{V} (the angular velocity is irrelevant since collisions are now treated as central) [47].

The choice between no-slip and slip BC is directly connected to the way the axis of colloids \mathbf{n}_i is evolved. In the first case, the solvent-disk interaction determines directly through torque exchange how colloids diffuse rotationally. In the second case, the rotational diffusion is accounted independently using Eq.(3). In this paper we choose the slip thermal BC for two reasons. The first one is that in this way we can choose the value of D_θ independently and match it with the one used in the ABP model. The second reason is that the integration of slip conditions is much faster than no-slip ones, since there is no need of considering the integration of disks angular velocities.

Since we will mostly deal with non-equilibrium simulations, solvent particles must be coupled to a thermostat to maintain constant temperature. We use the method of locally

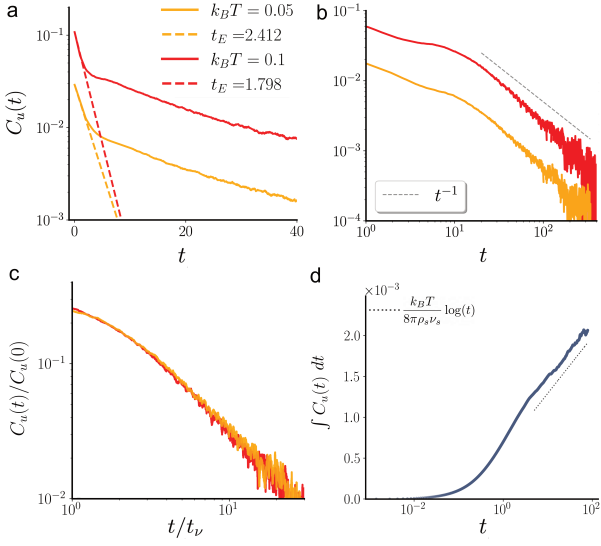


Fig. 2 VACF for different values of the temperature $k_B T$. Panels (a-c) show the VACF for the values $k_B T = 0.05$ (red curves) and $k_B T = 0.1$ (yellow curves), for the same number of solvent particles per cell $n_s = 10$. For short times (a), the autocorrelation function shows a clear exponential decay, which overlaps well with the theoretical prediction of the Enskog time t_E shown as dashed line for each case. At late times (b) simulations show a long time tail t^{-1} (dotted line in panel (b)). All the data collapse to the same curve if time is rescaled by t_v (c). (d) Time evolution, in semi-logarithmic scale, of the diffusion coefficient computed from the integral of the VACF, for the same parameters of the yellow curves of panel (a). The dotted line has the slope $\frac{k_B T}{8\pi\rho_s v_s}$.

rescaling fluid particles velocities \mathbf{v}_i relative to the centre of mass velocity \mathbf{u} for each cell by a proper factor that enforces the correct temperature [60]. We do not expect that this approach may alter flow profiles since, as later shown, we will adopt a very small cell size σ_s compared to variations in flow patterns and a very large value of n_s , the average number of solvent particles per cell. Note that this implementation ensures only local linear momentum conservation, while angular and total linear momenta are not conserved, as typically ensured in simulations of swimmers [44].

2.2.3 Parameter choice

In the case of the MPC fluid, an additional set of simulation parameters has to be set – n_s , m_s , σ_s , α , Δt_s – which will be expressed in terms of the colloids units – \tilde{m} , $\tilde{\sigma}$, $\tilde{\epsilon}$. In order to decide the MPC parameter values, a set of criteria, listed below, has to be satisfied.

The first criterion is that the solvent has to behave as a fluid (we remind that MPC particles satisfy an ideal gas equation of state); for such purpose we need to have a Schmidt number $Sc \simeq 10^2 - 10^3$, typical of liquids [61]. The Schmidt number represents in fact the ratio between the rate of momentum diffusion and the rate of mass transfer, and for large values of Sc the dynamics resembles the one of a liquid [62].

Sc is defined as $Sc = v_s/D_s$. Values $Sc \sim O(10)$ can be obtained by requiring small values of λ and large rotation angle [62]. Note that the choice $\lambda < \sigma_s$ is known to break the Galilean invariance [63], although this problem is cured by implementing the random shift procedure [63] which is here implemented. By using the expressions of v_s and D_s in the limit of $\lambda/\sigma_s \ll 1$, we find that the Schmidt number depends only on the mean-free path and takes the simple form[61]:

$$Sc \simeq \frac{1}{12(\lambda/\sigma_s)^2}, \quad (13)$$

where the dependence on n_s and α has been omitted since the dominant contribution is with λ .

The second criterion is that we want to have the same value of the friction γ as in ABP simulations, where γ has the same role as in the Langevin equation. For the MPC dynamics, this formula is:

$$\gamma = C_{2D}\pi v_s \rho_s (\sigma_c/2), \quad (14)$$

where $\rho_s = n_s m_s / \sigma_s^2$ is the solvent density. The coefficient C_{2D} depends on dimensionality [64] and the MPC model considered[40]. We performed simulations measuring the velocity of a colloid dragged by a constant force along a direction in 2D and we fitted a value of $C_{2D} = 1.84 \pm 0.1$, using six different values of forces and averaging over ten realizations. It is evident that also the choice of γ depends directly only on λ , when all the other parameters are fixed.

Regarding the active force and the rotational diffusion of the colloids axis, we do not need any change in the parameters chosen for the ABP, as the active force and the rotational diffusion are the same as the ones described in the equation of motion of the ABP model (equation (3)). Thus, the Pe number depends only on the colloids parameters, and is already set.

The last criterion that we need to follow is to have a very low compressibility in presence of the active force, in order for the fluid to remain homogeneous during the time evolution. This criterion was discussed in [58,40]. The correct parameters to look at are the Mach number and the Pumping number. The Mach number Ma is given by the ratio between the average fluid velocity v_s due to the external forces (in our case due to activity) and the sound velocity $v_{\text{sound}} = \sqrt{2k_B T / m_s}$ inside the fluid:

$$Ma = \frac{v_s}{v_{\text{sound}}}. \quad (15)$$

Its value depends directly on flow velocity. In order to reduce compressibility effects of the MPC fluid it should be $Ma < 0.2$ [65,66]. The Pumping number Pu , instead, is the ratio between the active stationary colloid velocity F_{act}/γ and the fluid self-diffusion:

$$Pu = \frac{\sigma_c F_{\text{act}}}{6\gamma D_s}, \quad (16)$$

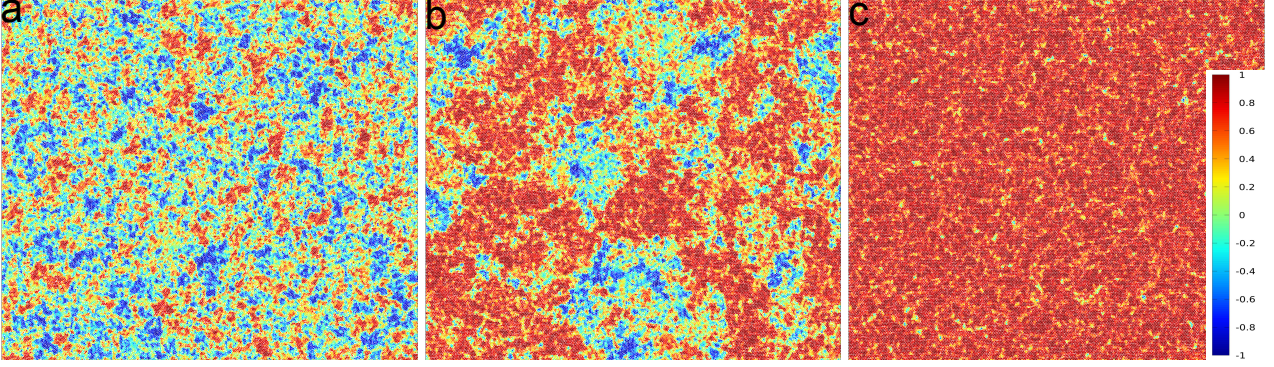


Fig. 3 Hexatic order parameter color map in the ABP model. (a)-(c) Color maps of the projection of the local hexatic order parameter of each particle, $\psi_{6,j}$, onto the direction of the system's global average, $\Psi = 1/N \sum_j \psi_{6,j}$, at fixed $Pe = 10$ and $m_c = 44$ for $\phi = 0.710, 0.730, 0.760$ respectively, for a system of size $L = 256\sigma_c$.

and should be less than 1 [40] in order for the fluid-particle diffusion to be faster than activity-induced advection, thus avoiding strong density inhomogeneities in the fluid.

Following these criteria, we chose the cell size to be $\sigma_s = 0.2\sigma_c$. This guarantees that there is a sufficiently large number of cells covering a colloid [59]. We fix $\alpha = \pi/2$, $m_s = 0.15$ and $n_s = 15$ for the fluid. Typically the colloids and solvent mass density should match in order for the colloids to be buoyant, so we set $m_c = 44.15$ such that $n_s m_s / \sigma_s^2 = 4m_c / (\pi\sigma_c^2)$. This choice provides a good compromise between avoiding compressibility effects[44], which for example arises if we choose lower n_s , and computational cost, which arises with higher values of n_s . We use as $\Delta t_c = 10^{-4}$ and $\Delta t_s = 410\Delta t_c$. The temperature T for the solvent and the other parameters relative to the active force and rotational diffusion remain the same as the one used for ABP. These parameters lead to the required values of $\gamma = 10.04$ ($v_s = 0.061$ and $\rho_s = 56.24$), $Sc = 99.48$, $Ma = 0.1$ and $Pu = 0.9$ for the highest $Pe = 20$ value considered. We note that the Reynolds number of the fluid is given by

$$Re = u_0 \sigma_c / v_s = F_{act} \sigma_c / \gamma v_s = 6Pu D_s / v_s = 6Pu / Sc, \quad (17)$$

which is always much less than one for our choice of the parameters. Thus we are in the low Reynolds number regime.

We start from a close-packed initial configuration of particles positioned in a triangular lattice, forming a slab, and with the orientation of the self-propelled force uniformly distributed. The initial velocities of all particles (fluid particles and colloids) were extracted from a Gaussian distribution with zero mean and variance $k_B T / m_s$ and $k_B T / m_c$ for solvent particles and colloids, respectively. Given that all the MPC and MD parameters are the same we are able to consider the same exact active colloids system, except for the presence of long range hydrodynamic interactions. We fix the Péclet number to $Pe = 10$ and 20 , and vary the packing fraction ϕ between 0.60 and 0.88 , where the hexatic-liquid transition was found to be critical for $m_c = 1$ [8]. For each set of parameters a single realization was considered, run

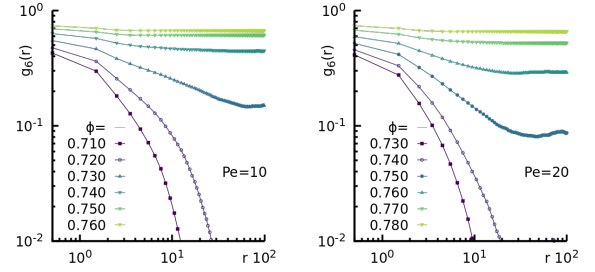


Fig. 4 Hexatic order correlation functions for the ABP model. Hexatic order correlation functions $g_6(r)$ for $m_c = 44$ at $Pe = 10$ (left) and $Pe = 20$ (right) for different global packing fractions given in the keys.

between 10^4 and 10^5 simulation time units after steady state was reached, and averaged quantities were performed during this time frame. To limit the computational cost for MPC simulations we always fix the box side to $L = 128\sigma_c$, unless otherwise specified.

2.3 Validation of slip boundary conditions

We focus here on the behaviour of passive colloids embedded in a solvent to test the accuracy of the previously described slip boundary conditions with respect to known results for 2D hydrodynamics. Following Ref. [67], we measure the velocity auto-correlation function (VACF) and the diffusion coefficient D_c of colloids. The parameters chosen for the simulation are the same as described in the previous section, except that we also varied either the average number of solvent particles per cell n_s or the temperature $k_B T$, always keeping the Schmidt number $Sc \simeq 100$. We considered large systems, with $L = 900\sigma_c$ to reduce periodic boundary effects.

At very short times, when hydrodynamics effects can be neglected, the main contribution to the overall diffusion comes from the local random collisions between colloid and

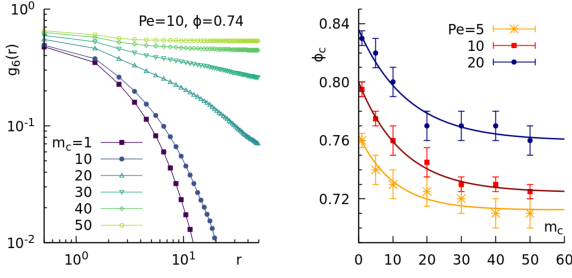


Fig. 5 Effects of colloids mass on the Liquid-Hexatic transition. On the left panel, orientational correlation functions, $g_6(r)$, at fixed $Pe = 10$ and $\phi = 0.74$ for different values of the mass of the particles given in the keys. On the right panel, the liquid-Hexatic critical density, ϕ_c , at fixed $Pe = 10$, as a function of the mass of the colloids m_c . The solid line is a fit of the data using the function $\phi_c(m_c) = a + be^{-m_c/c}$, with parameters $a = 0.71$, $b = 0.05$, $c = 10.37$ for $Pe = 5$; $a = 0.72$, $b = 0.08$, $c = 12.92$ for $Pe = 10$; and $a = 0.76$, $b = 0.08$, $c = 14.30$ for $Pe = 20$. The error bars correspond to the gap $\Delta\phi$ between the densities scanned in the simulations for each value of the mass m_c .

solvent particles. The VACF is given by

$$C_u(t) = \langle u(t)u(0) \rangle = \frac{k_B T}{m_c} \exp(-t/t_E), \quad (18)$$

where u is a Cartesian components (either x or y) of colloids velocity, $t_E = m_c/\xi$ is the Enskog time, that is the typical velocity decorrelation time, and ξ the Enskog friction coefficient given in two spatial dimensions by [67]

$$\xi = \frac{3\sqrt{2}}{4} \sigma_c n_s \pi^{3/2} \left(k_B T \frac{m_c m_s}{m_c + m_s} \right)^{1/2}. \quad (19)$$

The integral of the VACF is related to the diffusion coefficient D_c through the Green-Kubo relation,

$$D_c = \int_0^\infty \langle u(t)u(0) \rangle dt = \frac{k_B T}{\xi}. \quad (20)$$

However, as well known [68,69] fluid dynamic interactions have an important effect on the long-time behaviour of the VACF. Indeed, due to momentum conservation, the asymptotic form of the VACF shows an algebraic decay of the form

$$C_u(t) = \left(\frac{1}{2\rho_s} \right) \frac{k_B T}{[4\pi(D_c + v_s)t]}, \quad (21)$$

for slip boundary conditions in two dimensions. The VACF has a t^{-1} tail, meaning that the diffusion coefficient D_c diverges logarithmically with time. The long time tail can be expected to appear on the kinematic time scale $t_v = \sigma_c^2/v_s$, that is the time required by the kinematic viscosity v_s to diffuse over the colloid radius. We validate the slip coupling method introduced in Sec. 2.2.2 between solvent and passive colloids by testing these predictions.

Since the kinematic viscosity (9) depends only very weakly on n_s , for large values of n_s , and given that

$$C_u(0) = \frac{k_B T}{m_c}, \quad (22)$$

from equipartition, the long-time tails should all scale onto the same curve if time is rescaled by t_v .

Figure 1 shows the VACF for three different values of n_s and $k_B T = 0.1$. As shown in panels (a), for short times, the autocorrelation function shows clear exponential decay, while at late times (panels (b)-(c)) simulations show a long time tail t^{-1} . When plotted as functions of the reduced time t/t_v , all the data collapse onto the same curve (panel (c)). The oscillations visible in panels (b) and (c) for long times originate from sound modes and are a consequence of the finite compressibility of the MPC fluid combined with the periodic boundary conditions [70]. We checked that this effect decreases increasing the simulation box size.

The Enskog friction coefficient (19) slightly varies with n_s ; in order to test the sensibility of the implementation used we fixed $n_s = 10$

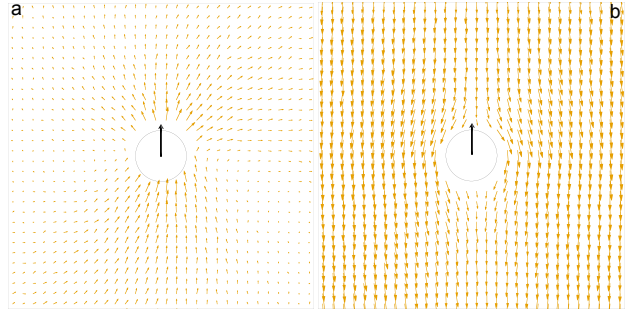


Fig. 6 Velocity field induced by an active colloid in the AHP model. Fluid velocity field around an active colloid for $Pe = 20$, in the lab frame (a) and in the colloid frame (b). The black arrow indicates the direction of the active force.

and varied the temperature to change the Enskog friction coefficient. Figure 2(a) shows the early time exponential decay of the VACF for the values $k_B T = 0.05, 0.1$. The measured values of t_E are in good agreement with the theoretical predictions. Also in this case the long-time tail has the expected t^{-1} slope (panel (b)), and all the curves collapse if time is rescaled by t/t_v (panel (c)).

Using the Green-Kubo relation, and Eq. (21), the diffusion coefficient can be approximated at long times, assuming that $D_c \ll v_s$ and that the Enskog and hydrodynamic contributions to the VACF can be separated, as

$$D_c(t) = \int_0^t \langle u(t)u(0) \rangle dt \approx \int_{t_v}^t \frac{k_B T}{8\pi\rho_s v_s t} dt \approx \frac{k_B T}{8\pi\rho_s v_s} [\ln t]_{t_v}^t. \quad (23)$$

Figure 2(d) shows the temporal evolution of the diffusion coefficient computed from the VACF. On the time scales of the simulation, we observe a behavior consistent with $D_c \simeq \ln(t)$, as expected from the t^{-1} tail of the VACF.

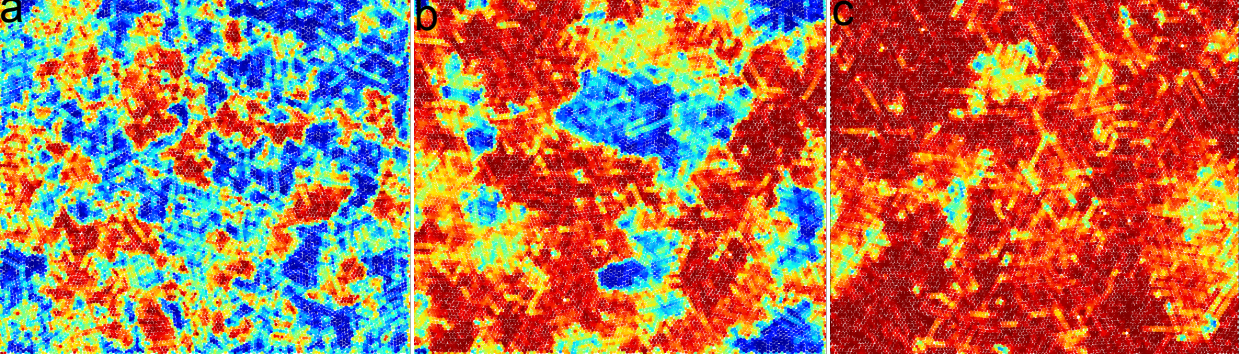


Fig. 7 Hexatic order parameter color map in the AHP model (a)-(c) Color maps of the local hexatic order parameter, $\psi_{6,j}$, as reported in Fig. 3, for $Pe = 10$ and $m_c = 44$, with $\phi = 0.78, 0.8, 0.81$ from left to right, for a system of size $L = 128\sigma_c$.

3 Hydrodynamic and variable mass effects on hexatic liquid transition

In this Section, we discuss the effects of changing the particles mass for the 2D ABP model and the role of hydrodynamics in the AHP model, using the numerical framework illustrated in the previous Section. In particular, we will focus onto characterizing the presence and location of the liquid-hexatic transition, by varying the system density in a region of the phase diagram at intermediate active forces where MIPS does not occur for over-damped ABP. The latter undergo the transition at $\phi_c = 0.795$ for $Pe = 10$ and at $\phi_c = 0.83$ for $Pe = 20$ [71].

The transition can be characterized by measuring the hexatic order parameter, $\psi_6(r_i) = \frac{1}{N_i} \sum_{j=1}^{N_i} e^{i6\theta_{ij}}$, with N_i the number of nearest Voronoi neighbours for particle i , and θ_{ij} the angle formed between the segment connecting particles i and j and the x -axis. From $\psi_6(r_i)$ we can compute the hexatic correlation function, defined as:

$$g_6(r) = \frac{\langle \psi_6(r_i) \psi_6(r_j) \rangle}{\langle \psi_6^2(r_i) \rangle}, \quad (24)$$

where $r = |\mathbf{r}_i - \mathbf{r}_j|$. The transition between hexatic and liquid phases can be observed by the change in the functional dependence of $g_6(r)$ from exponential decay for short-range order, $g_6(r) \sim e^{-r/l_c}$, where l_c is the correlation length, to algebraic for quasi-long-range order, $g_6(r) \sim r^{-\beta}$. We use henceforth this criteria to distinguish between the liquid and the hexatic phase in our system. In Sec. 3.2.1 we also discuss from a dynamical perspective how macroscopic flow properties emerge when hydrodynamics is considered.

3.1 Effects of different colloids mass in the ABP model

Here we characterize the evolution of ABP following the model described in Sec 2.1 at $Pe = 5, 10, 20$ and compare the results with the ones obtained in Ref. [71]. In particular, while in Ref. [71] only the value $m_c = 1$ was considered,

here we will study the system with various masses ranging from $m_c = 5$ to 50. Thus, the main difference is that here we are increasing the inertial time $t_I = m_c/\gamma$, ranging from $t_I = 0.5$ to 5 while maintaining the persistence time $t_p = 1/D_\theta \approx 67$ [1] constant, so that $7 \times 10^{-3} < pn < 7 \times 10^{-2}$. The use of large masses will allow a direct comparison with the AHP model (where $m_c = 44$) that will be used in the following.

We will focus on measuring approximately the value of the critical density ϕ_c where the liquid-hexatic transition occurs, computing the hexatic correlation at a fixed Pe within intervals of ϕ ranging from 0.05 to 0.1.

Fig. 3(a)-(c) show typical configurations at $Pe = 10$, $m_c = 44$ and three different densities. Configurations are colored according to the local hexatic parameter $\psi_{6,j}$, projected onto its average value. In panel (a) ($\phi = 0.71$) we do not observe the appearance of any macroscopic hexatic domain, while in panel c ($\phi = 0.76$) we observe a fully hexatically ordered system. Panel (b), with $\phi = 0.73$, is an intermediate density where macroscopic and orientationally ordered domains emerge, suggesting that this density is close to the transition point.

In order to locate the liquid-hexatic transition point at a fixed activity, we resort to study the hexatic correlation functions, finding the density at which these functions change from exponential to algebraic decay. Fig.4 shows these functions for $m_c = 44$ and $Pe = 10, 20$. At densities below $\phi = 0.72$ for $Pe = 10$ and $\phi = 0.74$ for $Pe = 20$, we find that the correlations have an exponential decay, while for larger values the behaviours that best fits the decay is that of an algebraic function. Thus, we find that at both activity considered the values where the liquid-hexatic transition occurs are lowered with respect to the ones at $m_c = 1$ reported in Ref. [28], suggesting that the increase in mass enhances the orientational ordering at fixed activity. In particular, we estimate $\phi_c = 0.730 \pm 0.01$ and 0.760 ± 0.01 for $Pe = 10, 20$, respectively.

We also checked that this ordering effect occurs while fixing the system density and activity, and increasing the colloids mass. The correlation functions in Fig. 5, left side,

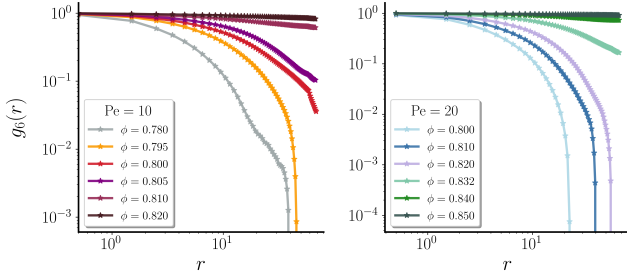


Fig. 8 Hexatic order correlation function for the AHP model. (a)-(b) Hexatic order correlation function $g_6(r)$ at $Pe = 10$ (d) and $Pe = 20$ (e) for different global packing fractions given in the keys and $m_c = 44$.

at $Pe = 10$ and $\phi = 0.74$, show that by increasing the mass the system crosses from a liquid state to a hexatic one. We summarize these measurements in the right panel of Fig. 5, where we show the location of the critical density for different Pe and different m_c . It is evident that the critical density of the liquid-hexatic transition continuously decreases increasing the value of the mass for the different Pe considered. Interestingly, the data fit with the function $\phi_c(m_c) = a + be^{-m_c/c}$, with coefficients reported in the caption.

To summarize, the results showed here point out that an enlarged mass, and therefore an increase in the inertial time t_I , has an effect of enhancing the orientational ordering of the system. It is important to note that this is a non-equilibrium effect not present in the passive system. Indeed, we checked (not shown) that in the absence of activity the transition density value is independent of the mass value. We also observed that the asymptotic values for large m_c (coefficient a in the fitting function) are close to the transition density at $Pe = 0$ [71]. When the persistence number is $pn \gtrsim 10^{-2}$ ($m_c \approx 10$), the system behaves closer to the passive case. On the other hand, when $pn \lesssim 10^{-2}$ the active force has a disordering effect in the hexatic ordering.

3.2 Hydrodynamics effects

We now turn our attention to the role of hydrodynamics by studying the AHP model. To do so, we employ the hybrid mesoscopic approach presented and tested in section 2, where the MPC solvent is coupled with the active colloids to account for hydrodynamic interactions. It is important to stress that in our numerical model no tangential flow velocity is imposed to colloids (they are not squirmers), thus the resulting velocity field is the result of collisions between moving colloids and fluid particles. In Fig. 6 we show the velocity field of our active colloid immersed in a fluid. The flow field strongly resembles that of a neutral swimmer.

The parameters of AHP, chosen in order to fulfil the constraints discussed in Sec. 2.2.3, fix the colloid mass to $m_c = 44$ and $\gamma = 10$. In this way, the AHP simulation results

can be directly compared with the ones of ABP with the same m_c . We will scan values of ϕ between 0.5 and 0.85.

3.2.1 Liquid-hexatic transition

We start by looking at how the ordering properties are affected by hydrodynamics. Fig. 7(a)-(c) show, for three different densities at $Pe = 10$, the color map of the local hexatic parameter $\psi_{6,j}$ projected onto its average value. In panel (a) ($\phi = 0.78$) we do not observe the appearance of macroscopic hexatic domains, but locally we still observe small orientationally ordered regions. These regions appear to become larger upon increasing the density (panel (b), $\phi = 0.8$), although global ordering is not observed. At $\phi = 0.81$, panel (c), a single fully hexatically ordered system is observed. Thus, also AHP present a transition between liquid and hexatic phases.

Fig. 8 shows the hexatic correlation functions varying the density for $Pe = 10, 20$, to be compared with the results presented in Fig. 4 for the ABP system. For both values of activity, we find that the hexatic order correlation function shift from an exponential decay to a power-law decay at substantially higher values of packing fraction ϕ . More precisely the transition is located at $\phi_c \approx 0.805 \pm 0.01$ for $Pe = 10$, and $\phi_c \approx 0.840 \pm 0.01$ for $Pe = 20$.

The increase in value of the transition density ϕ_c with respect to the ABP model suggests that the addition of hydrodynamic interactions has a disordering net effect regarding the global orientational order. This is opposite to the effect of increasing the particles mass, which instead promotes hexatic ordering. Indeed, if we measure the average global hexatic parameter $\psi_6 = \frac{1}{N} |\sum_i^N \psi_{6,i}|$ as a function of the global packing fraction ϕ (Fig. 9), which increases from 0 to 1 as the liquid-hexatic transition is crossed we find that the transition is significantly shifted. Note that both curves converge to almost the same values for very high densities, suggesting that for densely packed systems hydrodynamic does not disrupt the ordering properties of colloids.

We also checked (not shown) that in the absence of activity, the transition density values that limit the coexistence region of the liquid-hexatic transition of passive colloids [8] are not affected by the presence of hydrodynamic interactions. However, hydrodynamics produces other relevant effects which will be now discussed.

3.2.2 Self sustained motion at high density

We now want to better understand the behavior and the role of the fluid velocity field, which for AHP can be locally organized, while the ABP model has no such feature, and rely only on hard-core repulsion. Thus, we will have a deeper look into the velocity field of AHP, and if it can trigger a coherent motion of small clusters of particles.

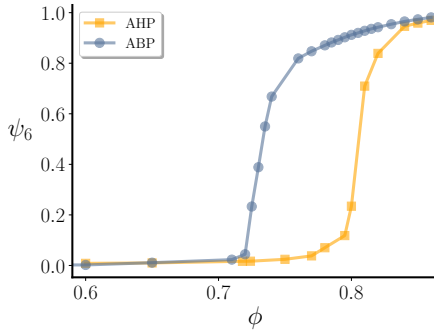


Fig. 9 Liquid-Hexatic transition in the ABP and AHP model. Global hexatic parameter as a function of the global packing fraction for $Pe = 10$ and $m_c = 44$. The orange and blue curves correspond to simulations with and without hydrodynamics, respectively, for active colloids with the same mass.

Fig. 10 shows the coarse-grained steady state velocity fields of the fluid, $\mathbf{v}(\mathbf{r})$ (panels d-f) along with associated snapshots of the configurations colored according to the hexatic parameter (panels a-c), for AHP with $Pe = 10$ and three different values of packing fraction ϕ . Coarse-grained velocity fields of the fluid are realized by averaging the velocity of fluid particles inside blocks of size $4\sigma_c = 20\sigma_s$ (such large coarse-graining cells are chosen for the sake of visualization; similar profiles can be obtained with smaller cells). The first density, $\phi = 0.60$ (panels (a), (d)), is characterized by the absence of any orientational order. At the same time, however, its corresponding velocity field presents the formation of vortices along with regions where flow is both not correlated and lower in magnitude. The associated velocity field for the active colloids (not shown) has a matching profile, while the local average direction of the active force is random, and thus not coherent with the velocity field.

Fig. 10b,e show instead a larger density $\phi = 0.80$. We observe, here, a case close to the hexatic transition point, with locally formed fluctuating hexatic domains with their typical size remaining stationary over time. Along with these clusters, the flow becomes more coherent than at $\phi = 0.60$, with fluid and colloids having again a similar velocity field. Again, we do not observe a local average direction of the active force coherent with the flow field. The same behaviour becomes even more pronounced upon increasing the density ($\phi = 0.860$ panels (c) and (f)), where the system is fully orientationally ordered. In this case, the associated flow field becomes an unidirected self-sustained flow, with particles moving typically on the same direction, and with the global direction of the flow slowly changing over time. Interestingly, this behaviour is similar to travelling bands occurring in Vicsek-like models [72,73], where an additional alignment interaction of active force directions is introduced, which allows particles to move coherently. Velocity correlations between particles have also been found in systems of ABP with different persistence times [74,75,76,77], flowing crys-

tals made of spontaneously aligning self-propelled hard disks [78] and self-sustained spontaneous flows in active gels [79, 80, 81, 82, 83].

We do not have at the moment a full theoretical understanding of the emergence of the coherent motion, which occurs even when there is no orientational ordering. We can only try to interpret the phenomenology in the following way: the self-propulsion force of colloids continuously injects energy into the fluid, setting it into motion. Fluid particles can later self-organize their motion in a coherent form, and drag colloids along their direction of motion, which is not necessarily the same direction of the active force of each particle.

A quantitative measure of this transition to unidirected self-sustained flow, as a synergetic effect of self-propulsion and hydrodynamic interactions, can be obtained by measuring the spatial velocity correlation function for the fluid velocity:

$$C_v(\mathbf{r}) = \frac{\langle \mathbf{v}(\mathbf{r})\mathbf{v}(\mathbf{0}) \rangle}{\langle \mathbf{v}(\mathbf{0})^2 \rangle}. \quad (25)$$

Fig. 11 shows $C_v(\mathbf{r})$ for different values of ϕ , for $Pe = 10$. For low values of ϕ (see e.g. $\phi = 0.600$) the curve shows an exponential decay. This corresponds to the case shown in Fig. 10(d), characterized by the presence of isolated vortices. When we increase the density, we observe that the velocity correlation has a slower decay, or a longer correlation length. Above density $\phi \simeq 0.730$, the correlation becomes almost constant. We note that the transition in the velocity correlations between exponential and algebraic decay does not manifest itself at the liquid-hexatic transition, since the latter appears at higher values of ϕ . In the inset of Fig. 11 the velocity correlation function for ABP in the hexatic phase ($Pe = 10$ and $\phi = 0.760$) is also shown for comparison. It shortly decays to zero, while for AHP, even in the liquid case (yellow curve), the decay is much slower. To gain more insights on the effects of hydrodynamic interactions we report the radial distribution function $g(r)$ in Fig. 12, for $\phi = 0.750$ both for ABP and AHP at $Pe = 10$. We observe that the presence of fluid in AHP does not considerably change the position of the peaks in the radial distribution function. However, we notice that the intensity of the peaks is enhanced in the ABP case, meaning that the fluid interferes with ordering, thus shifting the hexatic transition to higher densities.

As a last check, we switched off/on hydrodynamics by just removing/adding the solvent particles and adding/removing the Langevin friction and noise terms in the colloids equation of motion (3). This enables us to check if a stationary AHP configuration is naturally able to relax to a stationary conformation of the ABP when hydrodynamics is switched off. We choose $Pe = 10$ and $\phi = 0.795$, a density where the

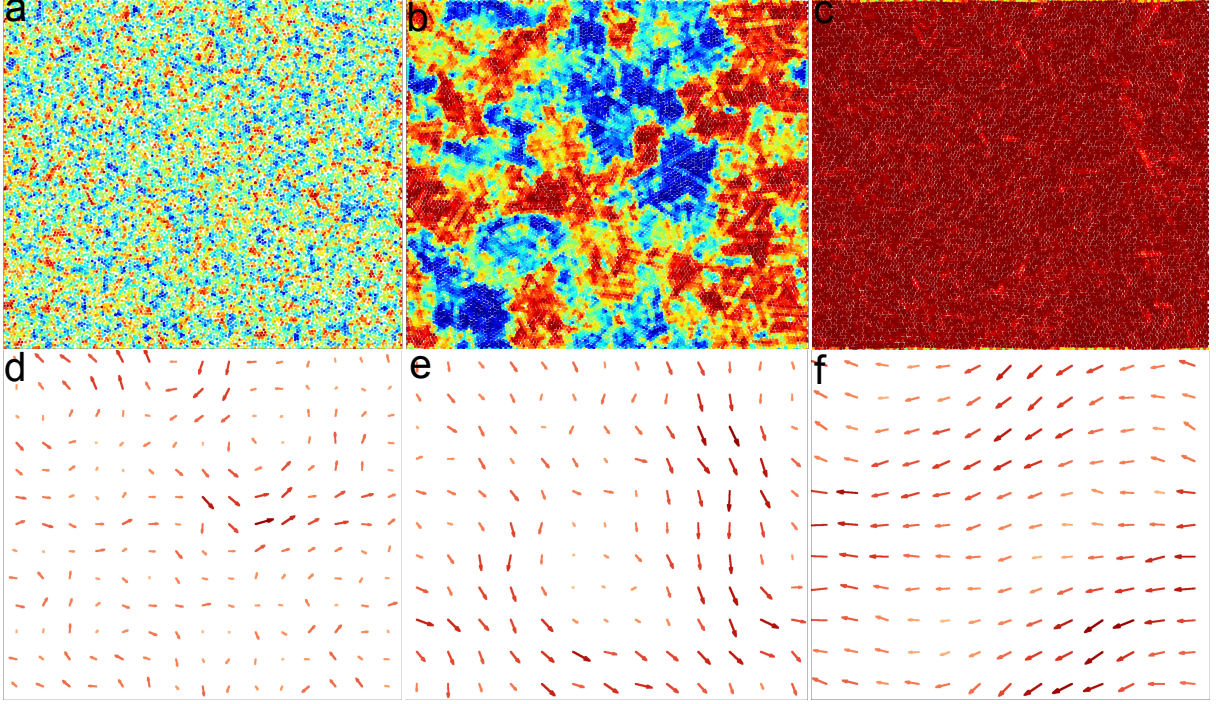


Fig. 10 Self-sustained active flow. (a)-(c) Color maps of the local hexatic order parameter for $Pe = 10$ and $\phi = 0.60, 0.80, 0.86$, respectively. Panels (d)-(f) show the corresponding steady state fluid velocity field. The color code is the same as the one in Fig. 3.

system is hexatically disordered/ordered with/without hydrodynamics. The results are shown in Fig. 13. We start with AHP in a fully ordered configuration; after an equilibration time of 10^4 simulation time units, the system forms fluctuating ordered domains which change over time but do not grow in size (panel (a)). We then turn off hydrodynamics, and the system gradually sets after $t = 10^5$ simulation time units to a almost fully hexatically ordered conformation (panel (b)). The corresponding colloids velocity field is shown in panels (c)-(d). Note that the configuration is still not fully ordered only due to the large time required to relax to the fully ordered state; however we observe that the global hexatic parameter is steadily growing over time. Switching on hydrodynamics again the system returns to the configuration shown in Fig. 13(a).

4 Conclusions

We have studied with extensive simulations the role of particles mass and hydrodynamics in active colloids, and showed how they affect the liquid-hexatic transition in an intermediate activity regime in which MIPS does not occur yet ($Pe = 10, 20$).

We have first characterized the ABP by changing their mass, while maintaining the same Pe and D_θ , so that we have a non-trivial interplay between the inertial time and the persistence time $t_p = 1/D_\theta$. We showed that the critical density of the transition is shifted to a lower density upon

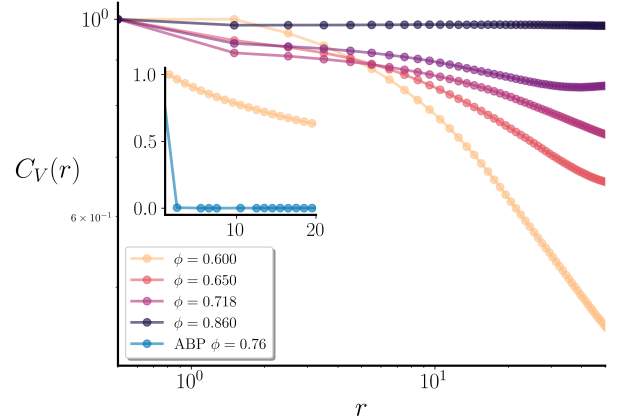


Fig. 11 Spatial velocity correlations. Spatial velocity correlation functions $C_V(r)$, for different values of ϕ , for $Pe = 10$. In the inset the velocity correlation function of ABP at $Pe = 10$ and $\phi = 0.760$ is compared with $\phi = 0.60$ for AHP at the same Pe .

increasing the colloid mass. This critical density is close to the one found at $Pe = 0$, suggesting that inertia has an orientational ordering effect on the system bringing the system closer to equilibrium behaviour and counteracting the disordering role of self-propulsion.

When hydrodynamic interactions are taken into account, we found instead that the liquid-hexatic transition moves towards higher values of packing fraction ϕ , thus suggesting that hydrodynamics has a net effect of orientationally disordering the system. We also analyzed the fluid velocity field

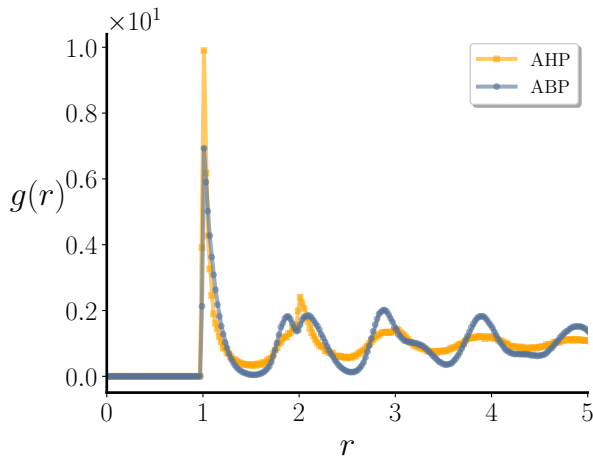


Fig. 12 Radial distribution function. Radial distribution function for ABP and AHP models with $\phi = 0.750$ at $Pe = 10$.

of AHP, and found at $Pe = 10$ two results: i) the formation below $\phi \approx 0.72$ of small correlated velocity field regions, characterized by the presence of vortices, that are not associated to any local orientational ordering; ii) the arising above $\phi \approx 0.720$ of a self-sustained motion, with the fluid particles moving in one direction. This change in behavior has been characterized by measuring the spatial velocity correlation which was found to change from an exponential to an algebraic decay.

Regarding the role of inertia, it will be interesting in the future to reconstruct a phase diagram similar to the one of Ref.[8], by characterizing in more detail the hexatic phase and the location of the solid phase. Regarding AHP, instead, it will be necessary to better describe the physical mechanisms producing the vortices at smaller densities and the transition to a self-sustained motion at larger densities. It remains an open question whether such a scenario is still encountered in quasi 2D and 3D geometries as well as in experiments with wet active colloids. It would also be of interest to investigate the effect of no-slip boundary conditions, which would completely determine the colloid angular diffusion and could induce additional cooperative effects, the effects of changing colloidal mass, and investigating in more details particle-particle flow interactions and local velocity field effects. We hope that our results can boost further research in this direction.

Acknowledgements

This work was possible thanks to the access to Bari ReCaS e-Infrastructure funded by MIUR through PON Research and Competitiveness 2007-2013 Call 254 Action I and MARCONI at CINECA (Project INF22-fieldturb) under CINECA-INFN agreement. We acknowledge funding from MIUR Project No. PRIN 2020/PFCXPE.

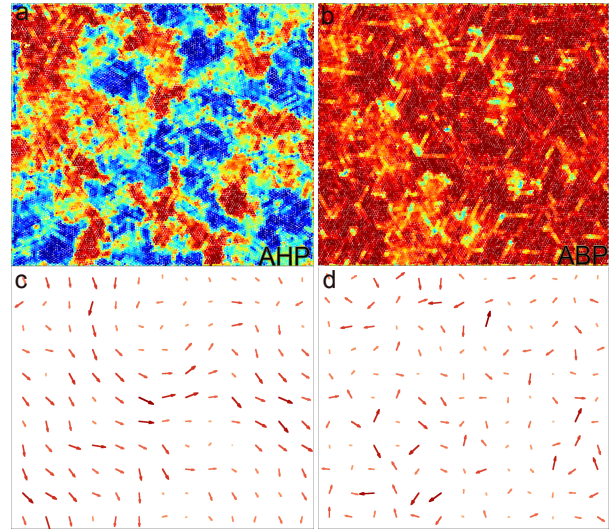


Fig. 13 Switch between ABP and AHP model. (a)-(b) Snapshots of the system at different times $t = 10^4, 10^5$ of the local hexatic order parameter, at $Pe = 10$ and $\phi = 0.795$, before (panel (a)) and after (panel (b)) switching off hydrodynamics. The corresponding colloids velocity fields are shown in panels (c)-(d).

Author contribution statement

All authors contributed equally to conceptualizing the research, analysing the results and writing the paper. GN and CBC carried out the simulations.

Data Availability Statement

The datasets generated during and/or analysed during the current study are available from the corresponding author on reasonable request.

References

1. Y. Fily and M.C. Marchetti. Athermal phase separation of self-propelled particles with no alignment. *Phys. Rev. Lett.*, 108:235702, Jun 2012.
2. P. Romanczuk, M. Bär, W. Ebeling, B. Lindner, and L. Schimansky-Geier. Active brownian particles. from individual to collective stochastic dynamics. *Eur. Phys. J. Spec. Top.*, 202:1–162, 2012.
3. J. Bialké, T. Speck, and H. Löwen. Crystallization in a dense suspension of self-propelled particles. *Phys. Rev. Lett.*, 108:168301, Apr 2012.
4. C. Bechinger, R. Di Leonardo, H. Löwen, C. Reichhardt, G. Volpe, and G. Volpe. Active particles in complex and crowded environments. *Rev. Mod. Phys.*, 88:045006, Nov 2016.
5. W. Bialek, A. Cavagna, I. Giardinà, T. Mora, E. Silvestri, M. Viale, and A.M. Walczak. Statistical mechanics for natural flocks of birds. *Proceedings of the National Academy of Sciences*, 109(13):4786–4791, 2012.
6. A.G. Be'er. A statistical physics view of swarming bacteria. *Mov. Ecol.*, 7, 2019.
7. D. Needleman and Z. Dogic. Active matter at the interface between materials science and cell biology. *Nat. Rev. Mater.*, 2, 2017.

8. P. Digregorio, D., A. Suma, L.F. Cugliandolo, G. Gonnella, and I. Pagonabarraga. Full phase diagram of active brownian disks: From melting to motility-induced phase separation. *Phys. Rev. Lett.*, 121:098003, Aug 2018.
9. C.B. Caporusso, P. Digregorio, D. Levis, L.F. Cugliandolo, and G. Gonnella. Motility-induced microphase and macrophase separation in a two-dimensional active brownian particle system. *Phys. Rev. Lett.*, 125:178004, Oct 2020.
10. M.E. Cates and J. Tailleur. Motility-induced phase separation. *Annual Review of Condensed Matter Physics*, 6(1):219–244, 2015.
11. G. Gonnella, D. Marenduzzo, A. Suma, and A. Tiribocchi. Motility-induced phase separation and coarsening in active matter. *Comptes Rendus Physique*, 16(3):316–331, 2015.
12. G.S. Redner, M.F. Hagan, and A. Baskaran. Structure and dynamics of a phase-separating active colloidal fluid. *Phys. Rev. Lett.*, 110:055701, Jan 2013.
13. I. Buttinoni, J. Bialké, F. Kümmel, H. Löwen, C. Bechinger, and T. Speck. Dynamical clustering and phase separation in suspensions of self-propelled colloidal particles. *Phys. Rev. Lett.*, 110:238301, Jun 2013.
14. F. Ginot, I. Theurkauff, D. Levis, C. Ybert, L. Bocquet, L. Berthier, and C. Cottin-Bizonne. Nonequilibrium equation of state in suspensions of active colloids. *Phys. Rev. X*, 5:011004, Jan 2015.
15. M. Rubenstein, A. Cornejo, and R. Nagpal. Programmable self-assembly in a thousand-robot swarm. *Science*, 345(6198):795–799, 2014.
16. P. Chvykov, T. A. Berrueta, A. Vardhan, W. Savoie, A. Samland, T. D. Murphey, K. Wiesenfeld, D.I. Goldman, and J.L. England. Low rattling: A predictive principle for self-organization in active collectives. *Science*, 371(6524):90–95, 2021.
17. S. Li, R. Batra, D. Brown, H. Chang, N. Ranganathan, C. Hoberman, D. Rus, and H. Lipson. Particle robotics based on statistical mechanics of loosely coupled components. *Nature*, 567(7748):361–365, 2019.
18. R. Kapral. Perspective: Nanomotors without moving parts that propel themselves in solution. *The Journal of Chemical Physics*, 138(2):020901, 2013.
19. Y. Katz, K. Tunström, C.C. Ioannou, C. Huepe, and I.D. Couzin. Inferring the structure and dynamics of interactions in schooling fish. *Proceedings of the National Academy of Sciences*, 108(46):18720–18725, 2011.
20. A. Celani, K. Gustavsson, L. Biferale, and S. Colabrese. Finding efficient swimming strategies in a three-dimensional chaotic flow by reinforcement learning. *Eur. Phys. J. E*, 40(110), 2017.
21. A. Doostmohammadi and J.M. Yeomans. Coherent motion of dense active matter. *Eur. Phys. J. Spec. Top.*, 227:2401–2411, 2019.
22. E. Tjhung and L. Berthier. Analogies between growing dense active matter and soft driven glasses. *Phys. Rev. Research*, 2:043334, Dec 2020.
23. R. Mandal, P.J. Bhuyan, P. Chaudhuri, C. Dasgupta, and M. Rao. Extreme active matter at high densities. *Nat Commun*, 11, 2020.
24. S. Henkes, K. Kostanjevec, J.M. Collinson, R. Sknepnek, and E. Bertin. Dense active matter model of motion patterns in confluent cell monolayers. *Nat Commun*, 11, 2020.
25. D. Bi, X. Yang, M.C. Marchetti, and M.L. Manning. Motility-driven glass and jamming transitions in biological tissues. *Phys. Rev. X*, 6:021011, Apr 2016.
26. J. Yan, M. Han, J. Zhang, C. Xu, E. Luijten, and S. Granick. Reconfiguring active particles by electrostatic imbalance. *Nature Mater*, 15:1095–1099, 2016.
27. J.U. Klamser, S.C. Kapfer, and W. Krauth. Thermodynamic phases in two-dimensional active matter. *Nat Commun*, 9, 2018.
28. P. Digregorio, D. Levis, L.F. Cugliandolo, G. Gonnella, and I. Pagonabarraga. Unified analysis of topological defects in 2d systems of active and passive disks. *Soft Matter*, 18:566–591, 2022.
29. E.P. Bernard and W. Krauth. Two-step melting in two dimensions: First-order liquid-hexatic transition. *Phys. Rev. Lett.*, 107:155704, Oct 2011.
30. S.C. Kapfer and W. Krauth. Two-dimensional melting: From liquid-hexatic coexistence to continuous transitions. *Phys. Rev. Lett.*, 114:035702, Jan 2015.
31. A.L. Thorneywork, J.L. Abbott, Dirk G. A. L. D.G.A.L. Aarts, and R.P.A. Dullens. Two-dimensional melting of colloidal hard spheres. *Phys. Rev. Lett.*, 118:158001, Apr 2017.
32. J.M. Kosterlitz and D.J. Thouless. Ordering, metastability and phase transitions in two-dimensional systems. *Journal of Physics C: Solid State Physics*, 6(7):1181–1203, apr 1973.
33. B.I. Halperin and D.R. Nelson. Theory of two-dimensional melting. *Phys. Rev. Lett.*, 41:121–124, Jul 1978.
34. A.P. Young. Melting and the vector coulomb gas in two dimensions. *Phys. Rev. B*, 19:1855–1866, Feb 1979.
35. P. Nie, J. Chattoraj, A. Piscitelli, P. Doyle, R. Ni, and M.P. Ciamarra. Stability phase diagram of active brownian particles. *Phys. Rev. Research*, 2:023010, Apr 2020.
36. L. Caprini and U.M.B. Marconi. Inertial self-propelled particles. *The Journal of Chemical Physics*, 154(2):024902, 2021.
37. A.K. Omar, K. Klymko, T. GrandPre, P.L. Geissler, and J.F. Brady. Tuning nonequilibrium phase transitions with inertia. *arXiv:2108.10278*, 2021.
38. I. Petrelli, L.F. Cugliandolo, G. Gonnella, and A. Suma. Effective temperatures in inhomogeneous passive and active bidimensional brownian particle systems. *Phys. Rev. E*, 102:012609, Jul 2020.
39. H. Löwen. Inertial effects of self-propelled particles: From active brownian to active langevin motion. *The Journal of Chemical Physics*, 152(4):040901, 2020.
40. M. Theers, E. Westphal, K. Qi, R.G. Winkler, and G. Gompper. Clustering of microswimmers: interplay of shape and hydrodynamics. *Soft Matter*, 14:8590–8603, 2018.
41. R. Matas-Navarro, R. Golestanian, T.B. Liverpool, and S.M. Fielding. Hydrodynamic suppression of phase separation in active suspensions. *Phys. Rev. E*, 90:032304, Sep 2014.
42. G. Gompper, R.G. Winkler, T. Speck, A. Solon, C. Nardini, F. Peruani, H. Löwen, R. Golestanian, U.B. Kaupp, L. Alvarez, T. Kjørboe, E. Lauga, W.C.K. Poon, A. DeSimone, S. Muiños-Landin, A. Fischer, N.A. Söker, F. Cichos, R. Kapral, P. Gaspard, M. Ripoll, F. Sagues, A. Doostmohammadi, J.M. Yeomans, I.S. Aranson, C. Bechinger, H. Stark, C.K. Hemelrijk, F.J. Nedelec, T. Sarkar, T. Aryaksama, M. Lacroix, G. Duclos, V. Yashunsky, P. Silberzan, M. Arroyo, and S. Kale. The 2020 motile active matter roadmap. *Journal of Physics: Condensed Matter*, 32(19):193001, feb 2020.
43. A. Zöttl and H. Stark. Hydrodynamics determines collective motion and phase behavior of active colloids in quasi-two-dimensional confinement. *Phys. Rev. Lett.*, 112:118101, Mar 2014.
44. M. Theers, Westphal E, K. Qi, R.G. Winkler, and G. Gompper. Clustering of microswimmers: interplay of shape and hydrodynamics. *Soft Matter*, 14:8590–8603, 2018.
45. A. Malevanets and R. Kapral. Mesoscopic model for solvent dynamics. *The Journal of Chemical Physics*, 110(17):8605–8613, 1999.
46. G. Gompper, T. Ihle, D.M. Kroll, and R.G. Winkler. *Multi-Particle Collision Dynamics: A Particle-Based Mesoscale Simulation Approach to the Hydrodynamics of Complex Fluids*, pages 1–87. Springer Berlin Heidelberg, Berlin, Heidelberg, 2009.
47. D.S. Bolintineanu, G.S. Grest, J.B. Lechman, F. Pierce, S.J. Plimpton, and P.R. Schunk. Particle dynamics modeling methods for colloid suspensions. *Computational Particle Mechanics*, 1(3):321–356, 2014.
48. A. Suma, G. Gonnella, G. Laghezza, A. Lamura, A. Mossa, and L.F. Cugliandolo. Dynamics of a homogeneous active dumbbell system. *Phys. Rev. E*, 90:052130, Nov 2014.

49. S. Plimpton. Fast parallel algorithms for short-range molecular dynamics. *Journal of Computational Physics*, 117(1):1–19, 1995.
50. A. Malevanets and R. Kapral. Solute molecular dynamics in a mesoscale solvent. *The Journal of Chemical Physics*, 112(16):7260–7269, 2000.
51. N. Kikuchi, C.M. Pooley, J.F. Ryder, and J.M. Yeomans. Transport coefficients of a mesoscopic fluid dynamics model. *The Journal of Chemical Physics*, 119(12):6388–6395, 2003.
52. T. Ihle, E. Tüzel, and D.M. Kroll. Resummed green-kubo relations for a fluctuating fluid-particle model. *Phys. Rev. E*, 70:035701, Sep 2004.
53. E. Tüzel, T. Ihle, and D.M. Kroll. Dynamic correlations in stochastic rotation dynamics. *Phys. Rev. E*, 74:056702, Nov 2006.
54. L. Bocquet and J. Barrat. Hydrodynamic boundary conditions, correlation functions, and kubo relations for confined fluids. *Phys. Rev. E*, 49:3079–3092, Apr 1994.
55. Y. Inoue, Y. Chen, and H. Ohashi. Development of a simulation model for solid objects suspended in a fluctuating fluid. *Journal of Statistical Physics*, 107(1):85–100, 2002.
56. A. Lamura, G. Gompper, T. Ihle, and D.M. Kroll. Multi-particle collision dynamics: Flow around a circular and a square cylinder. *Europhysics Letters (EPL)*, 56(3):319–325, nov 2001.
57. J.T. Padding, A. Wysocki, H. Löwen, and A.A. Louis. Stick boundary conditions and rotational velocity auto-correlation functions for colloidal particles in a coarse-grained representation of the solvent. *Journal of Physics: Condensed Matter*, 17(45):S3393–S3399, oct 2005.
58. J.T. Padding and A.A. Louis. Hydrodynamic interactions and brownian forces in colloidal suspensions: Coarse-graining over time and length scales. *Phys. Rev. E*, 74:031402, Sep 2006.
59. M. Hecht, J. Harting, T. Ihle, and H.J. Herrmann. Simulation of claylike colloids. *Phys. Rev. E*, 72:011408, Jul 2005.
60. H. Chien-Cheng, A. Varghese, G. Gompper, and R.G. Winkler. Thermostat for nonequilibrium multiparticle-collision-dynamics simulations. *Phys. Rev. E*, 91:013310, Jan 2015.
61. M. Ripoll, K. Mussawisade, R.G. Winkler, and G. Gompper. Low-reynolds-number hydrodynamics of complex fluids by multi-particle-collision dynamics. *Europhysics Letters (EPL)*, 68(1):106–112, oct 2004.
62. M. Ripoll, K. Mussawisade, R.G. Winkler, and G. Gompper. Dynamic regimes of fluids simulated by multiparticle-collision dynamics. *Phys. Rev. E*, 72:016701, Jul 2005.
63. O.M. Braun and M. Peyrard. Friction in a solid lubricant film. *Phys. Rev. E*, 63:046110, Mar 2001.
64. B. Liu, J. Goree, and O.S. Vaulina. Test of the stokes-einstein relation in a two-dimensional yukawa liquid. *Phys. Rev. Lett.*, 96:015005, Jan 2006.
65. A. Lamura and G. Gompper. Numerical study of the flow around a cylinder using multi-particle collision dynamics. *Eur. Phys. J. E*, 9(5):477–485, 2002.
66. E. Guyon, J.P. Hulin, L. Petit, and C.D. Matescu. *Physical Hydrodynamics*. Oxford University Press, 2015.
67. J.T. Padding J. Sané and A.A. Louis. Hydrodynamics of confined colloidal fluids in two dimensions. *Phys. Rev. E*, 79:051402, May 2009.
68. B.J. Alder and T.E. Wainwright. Decay of the velocity autocorrelation function. *Phys. Rev. A*, 1:18–21, Jan 1970.
69. M.H. Ernst, E.H. Hauge, and J.M.J. van Leeuwen. Asymptotic time behavior of correlation functions. *Phys. Rev. Lett.*, 25:1254–1256, Nov 1970.
70. C. Huang, G. Gompper, and R.G. Winkler. Hydrodynamic correlations in multiparticle collision dynamics fluids. *Phys. Rev. E*, 86:056711, Nov 2012.
71. L.F. Cugliandolo, P. Digregorio, G. Gonnella, and A. Suma. Phase coexistence in two-dimensional passive and active dumbbell systems. *Phys. Rev. Lett.*, 119:268002, Dec 2017.
72. V. Tamás and A. Zafeiris. Collective motion. *Physics Reports*, 517(3):71–140, 2012. Collective motion.
73. A. Martín-Gómez, D. Levis, A. Díaz-Guilera, and I. Pagonabarraga. Collective motion of active brownian particles with polar alignment. *Soft Matter*, 14:2610–2618, 2018.
74. L. Caprini, U.M.B. Marconi, and A. Puglisi. Spontaneous velocity alignment in motility-induced phase separation. *Phys. Rev. Lett.*, 124:078001, Feb 2020.
75. L. Caprini, U.M.B. Marconi, C. Maggi, M. Paoluzzi, and A. Puglisi. Hidden velocity ordering in dense suspensions of self-propelled disks. *Phys. Rev. Research*, 2:023321, Jun 2020.
76. U.M.B. Marconi, L. Caprini, and A. Puglisi. Hydrodynamics of simple active liquids: the emergence of velocity correlations. *New Journal of Physics*, 23(10):103024, oct 2021.
77. L. Caprini and U.M.B. Marconi. Spatial velocity correlations in inertial systems of active brownian particles. *Soft Matter*, 17:4109–4121, 2021.
78. G. Briand, M. Schindler, and O. Dauchot. Spontaneously flowing crystal of self-propelled particles. *Phys. Rev. Lett.*, 120:208001, May 2018.
79. L.N. Carenza, G. Gonnella, A. Lamura, G. Negro, and A. Tiribocchi. Lattice boltzmann methods and active fluids. *Eur. Phys. J. E*, 42(6):81, 2019.
80. G. Negro, L.N. Carenza, A. Lamura, A. Tiribocchi, and G. Gonnella. Rheology of active polar emulsions: from linear to unidirectional and inviscid flow, and intermittent viscosity. *Soft Matter*, 15:8251–8265, 2019.
81. M.G. Giordano, F. Bonelli, L.N. Carenza, G. Gonnella, and G. Negro. Activity-induced isotropic-polar transition in active liquid crystals. *EPL (Europhysics Letters)*, 133(5):58004, mar 2021.
82. L. N. Carenza, G. Gonnella, A. Lamura, D. Marenduzzo, G. Negro, and A. Tiribocchi. Soft channel formation and symmetry breaking in exotic active emulsions. *Scientific Reports*, 10(1):15936, 2020.
83. G. Negro, A. Lamura, G. Gonnella, and D. Marenduzzo. Hydrodynamics of contraction-based motility in a compressible active fluid. *EPL (Europhysics Letters)*, 127(5):58001, oct 2019.